Earth and Planetary Science Letters 327-328 (2012) 97–110

Contents lists available at SciVerse ScienceDirect

Earth and Planetary Science Letters

journal homepage: www.elsevier.com/locate/epsl

Spatiotemporal trends in erosion rates across a pronounced rainfall gradient: Examples from the southern Central Andes

Bodo Bookhagen [a,*], Manfred R. Strecker [b]

[a] Geography Department, Ellison Hall 1832, UC Santa Barbara, CA 93106-4060, USA
[b] Institute of Earth and Environmental Science, Universität Potsdam, Germany

ARTICLE INFO

Article history:
Accepted 9 February 2012
Available online 7 March 2012

Editor: T.M. Harrison

Keywords:
erosion
landscape evolution
specific stream power
cosmogenic radionuclides
paleoclimate
climate-tectonic feedback processes

ABSTRACT

The tectonic and climatic boundary conditions of the broken foreland and the orogen interior of the southern Central Andes of northwestern Argentina cause strong contrasts in elevation, rainfall, and surface-process regimes. The climatic gradient in this region ranges from the wet, windward eastern flanks (~2 m/yr rainfall) to progressively drier western basins and ranges (~0.1 m/yr) bordering the arid Altiplano–Puna Plateau. In this study, we analyze the impact of spatiotemporal climatic gradients on surface erosion: First, we present 41 new catchment-mean erosion rates derived from cosmogenic nuclide inventories to document spatial erosion patterns. Second, we re-evaluate paleoclimatic records from the Calchaquíes basin (66°W, 26°S), a large intermontane basin bordered by high (>4.5 km) mountain ranges, to demonstrate temporal variations in erosion rates associated with changing climatic boundary conditions during the late Pleistocene and Holocene. Three key observations in this region emphasize the importance of climatic parameters on the efficiency of surface processes in space and time: (1) First-order spatial patterns of erosion rates can be explained by a simple specific stream power (SSP) approach. We explicitly account for discharge by routing high-resolution, satellite derived rainfall. This is important as the steep climatic gradient results in a highly nonlinear relation between drainage area and discharge. This relation indicates that erosion rates (ER) scale with $ER \sim SSP^{1.4}$ on cosmogenic-nuclide time scales. (2) We identify an intrinsic channel-slope behavior in different climatic compartments. Channel slopes in dry areas (<0.25 m/yr rainfall) are slightly steeper than in wet areas (>0.75 m/yr) with equal drainage areas, thus compensating lower amounts of discharge with steeper slopes. (3) Erosion rates can vary by an order of magnitude between presently dry (~0.05 mm/yr) and well-defined late Pleistocene humid (~0.5 mm/yr) conditions within an intermontane basin. Overall, we document a strong climatic impact on erosion rates and channel slopes. We suggest that rainfall reaching areas with steeper channel slopes in the orogen interior during wetter climate periods results in intensified sediment mass transport, which is primarily responsible for maintaining the balance between surface uplift, erosion, sediment routing and transient storage in the orogen.

1. Introduction

During the past two decades research devoted to understanding the possible feedback mechanisms between tectonics and climate has suggested that focused erosion on the Earth's surface may influence crustal-scale deformation processes through the redistribution of mass and associated stress changes (Beaumont et al., 2001; Davis et al., 1983; Hilley and Coutand, 2010; Koons, 1989; Reiners et al., 2003; Thiede et al., 2004; Whipple, 2009; Willett, 1999). Erosion processes affecting Earth's surface can modify the distribution of lithostatic stresses through elevation changes (Dahlen, 1984; Hilley and Strecker, 2005; Molnar and England, 1990; Whipple and Meade, 2006) and thus may influence the locus of crustal deformation. However, in compressional mountain belts the destructive forces (i.e., erosion) act toward maintaining a balance with the constructive forces (i.e., tectonics) to ultimately achieve a steady-state system (e.g., Whipple, 2009; Willett and Brandon, 2002). In this context, steep climatic gradients associated with orographic rainfall and inferred high erosion rates on windward sides of mountain ranges have been used to explain crustal deformation patterns (e.g., Clift et al., 2008; Hodges et al., 2004; Koons, 1990; Masek et al., 1994; Strecker et al., 2007; Thiede et al., 2004), although this linkage is also debated (e.g., Burbank et al., 2003) and is complex (Thiede et al., 2009). The underlying key concept of a tectonics-climate feedback is that regions with similar geologic and topographic conditions erode and exhume faster during wetter conditions than under a dry climate regime.

Erosion and sediment transport are mainly a function of topography, climate, and lithology (e.g., Ahnert, 1970; Howard et al., 1994; Whipple, 2009). The limiting parameter controlling erosion, transient sediment storage, and ultimately, mass evacuation in a tectonically

* Corresponding author. Tel.: +1 805 893 3568; fax: +1 805 893 2578.
E-mail address: bodo@eri.ucsb.edu (B. Bookhagen).

0012-821X/$ – see front matter © 2012 Elsevier B.V. All rights reserved.
doi:10.1016/j.epsl.2012.02.005

Table 1
List of 41 river-sand samples, corresponding drainage basins, catchment locations, topographic and climatic 187 parameters, and catchment-mean erosion rates (see Fig. 1 for catchment locations).

Sample ID	River	Latitude (°S)[a]	Longitude (°W)[a]	Drainage area (km^2)	Mean basin elevation (km)	Mean 5-km-radius relief (km)	Mean hillslope angle (°)	Mean k_{sn} - drainage area[b]	Mean k_{sn} - TRMM discharge[c]
Calchaquies Basin									
STR-1	Rio de las Conchas (Metan)	−25.4678	−65.0556	163	1.36	0.95	11.8	101	90
STR-2	Rio San Antonio (N. Cafayate)	−25.8424	−66.0329	18	1.99	0.64	5.0	51	31
STR-3	Rio Blanco	−24.9910	−65.9731	314	3.32	1.27	12.4	108	46
STR-5	Quebrada de Escoipe (upper section)	−25.1860	−65.7881	332	2.77	1.61	20.2	141	46
STR-6	Quebrada de Escoipe (lower Section)	−25.1833	−65.7808	361	2.73	1.61	20.5	141	47
STR-9	Rio Aimacha	−26.7111	−65.8250	287	3.38	1.47	13.2	169	88
STR-10	Rio Salinas	−26.6226	−65.9670	24	1.96	0.32	3.5	29	22
STR-11	Rio Luracatao	−25.1486	−66.4906	1,387	4.00	1.60	17.4	173	67
STR-13	Rio Calchaquies	−24.7253	−66.2542	1,461	4.12	1.69	20.0	108	74
STR-16	Rio Tacuil	−25.5590	−66.5387	1,356	3.57	1.27	14.9	135	53
STR-17	Rio Laviña (W of Salta)	−25.4406	−65.7160	316	2.15	1.24	19.9	103	56
STR-19	Rio Laviña (Calchaquies Valley)	−25.8470	−66.1190	277	2.76	1.20	14.6	120	66
C1	Rio San Bernardo de las Zorras	−24.2305	−65.8737	1,666	3.82	1.15	13.7	100	42
C2	Rio Toro	−24.4070	−66.0198	493	3.76	1.25	15.1	118	49
C3	Quebrada Lampazar	−24.5057	−65.7601	137	3.55	1.32	12.5	127	49
C4	No name, south of Est. Maury	−24.3370	−65.8930	2,723	3.72	1.22	14.7	113	47
C5	Quebrada Incamayo	−24.5900	−65.7124	177	3.71	1.61	18.3	153	60
C6	Rio Toro, lower gorge	−24.7307	−65.9569	1,012	3.66	1.74	22.1	171	76
AFL	Rio Afluente	−24.7535	−65.6652	65	2.73	2.03	25.4	167	85
PORT	Rio Potrero	−24.6434	−65.6411	154	2.90	1.71	21.8	162	55
M1	Rio Juramento	−25.9354	−66.1673	33,308	2.93	1.17	13.3	116	61
M2	Rio Calchaquies (before Rio Santa Maria)	−25.4428	−66.2539	12,716	3.36	1.21	13.8	117	56
M3	Rio Santa Maria	−26.6698	−66.1597	6,094	3.05	1.04	10.4	107	58
Humahuaca Basin									
STR-8	Iturbe	−22.8771	−65.4491	786	3.87	0.68	10.7	55	31
STR-12	Rio Iruya	−22.8721	−65.2183	125	3.90	1.69	20.5	167	96
STR-14	Rio Sta Victoria between Iruya and Irtube	−22.8311	−65.3014	145	3.98	1.01	11.5	69	36
STR-21	Rio Grande	−23.3546	−65.4388	5,903	3.67	1.27	15.5	118	66
STR-22	A del Medio	−23.9399	−65.5435	21	3.45	2.20	30.0	173	65
STR-23	Rio Yacoraite	−23.2154	−65.5719	946	3.83	0.99	12.6	50	49
STR-24	Rio Grande	−23.1844	−65.3976	4,427	3.73	1.12	13.8	101	59
WIE	Rio Wierna	−24.5351	−65.5103	643	2.58	1.42	18.7	161	83
CALD	Rio Caldera	−24.5140	−65.4380	171	2.07	1.17	17.2	116	79
VAQU	Rio Vaqueros	−24.6609	−65.5202	128	2.07	1.33	17.6	129	88
ARG-13	Rio San Lorenzo	−23.5461	−65.0578	2,186	2.56	1.67	23.4	200	118
ARG-12	Rio Ledesma	−23.8772	−65.1832	14,064	1.82	1.18	17.1	141	103
Tucuman Basin									
STR-4	Rio Sali	−26.0533	−65.3606	1,794	1.28	0.67	9.1	65	51
STR-25	Rio Susa	−27.0572	−65.6146	47	0.82	1.14	11.9	115	106
STR-26	Rio Famailla	−26.9110	−65.5182	104	1.22	1.09	14.8	120	98
ARG-11	Rio Cachuma	−27.2717	−66.0325	206	3.14	2.32	24.4	307	159
ARG-27	Rio Alumbrera	−27.5726	−66.0619	634	2.05	0.91	9.7	69	49
Altiplano–Puna Basin									
STR-18	Salinas Grandes	−23.6504	−65.7302	18	3.88	0.68	8.1	51	21

[a] Centroid (center of gravity) of catchment polygon.
[b] Values were calculated with spatially uniform rainfall (i.e., 1 m/yr for each gridpoint in the basin).
[c] Values were calculated with calibrated satellite-derived rainfall from the TRMM (Tropical Rainfall Measurement Mission) platform, product 2B31.
[d] Rainfall amounts taken from TRMM product 2B31 (cf. Bookhagen and Burbank, 2010; Bookhagen and Strecker, 2008).
[e] Production rate calculation are performed for every gridpoint in a catchment at 250-m spatial resolution. Production rates depend on latitude, altitude, and explicitly includes muogenic production (Granger and Muzikar (2001) and uses a Lal (1991) scaling scheme with a HLSL production of 4.7 atoms g^{-1} yr^{-1} (Balco et al., 2009).
[f] Derived from blank-corrected AMS measurements undertaken at Lawrence Livermore National Laboratory and normalized to ICN standard (Nishiizumi et al., 2007).
[g] Denudation rates are calculated with a bedrock density of 2.6 g cm^{-3} and an attenuation length for spallation of $\lambda = 160$ g cm^2.

active mountain belt, is topographic relief together with lithology and climate (e.g., Ahnert, 1970; Whipple, 2009; Whipple et al., 1999). It has been long recognized that a first-order erosional response to an increase in tectonic forcing (and hence increase in relief) is the steepening of hillslopes, which results in more effective removal of material and an increase in erosion rates (e.g., Ahnert, 1970; Culling, 1960). However, hillslopes only steepen until reaching a threshold value above which erosion rates may increase via higher landslide frequency (Bookhagen et al., 2005b; Burbank et al., 1996; Hovius et al., 1997) or slope-length changes (Howard, 1994; Tucker and Bras, 1998). For example, studies in the San Bernadino and San Gabriel mountains of southern California (Binnie et al., 2007; DiBiase et al., 2010) suggest that catchment-mean hillslope gradients reach a maximum at erosion rates of ~0.2 mm/yr, implying that the frequency of landslides must increase to keep pace with tectonic forcing in excess of 0.2 mm/yr. Similar threshold concepts were developed in a variety of environments (e.g., Gilbert, 1877; Ahnert, 1970; Burbank et al., 1996; Montgomery and Brandon, 2002; Ouimet et al., 2009). Because of this threshold-hillslope behavior, additional topographic parameters have been evaluated to explain spatial erosion-rate variations. One

Mean specific stream power (W/m^2) - drainage area[b]	Mean specific stream power (W/m^2) - TRMM discharge[c]	Mean annual rainfall from calibrated TRMM (m/yr)[d]	Mean production rate (atoms/(g_{qtz} * yr))[e]	Number of atoms x10^3 (atoms/g_{qtz})[f]	Number of atoms x10^3 (1σ) (atoms/g_{qtz})	Denudation rate (μm/yr or mm/kyr)[g]	Denudation rate (1σ) (μm/yr or mm/kyr)	Apparent age (kyr)
37	30	1.04	10.0	5.74	0.79	1055	167.9	0.6
23	16	0.38	15.3	163.81	2.21	56	0.8	12.9
41	27	0.19	37.7	513.90	15.15	44	1.3	20.1
58	35	0.10	25.5	47.38	1.15	325	8.1	2.2
60	37	0.13	24.8	22.34	1.39	672	44.7	1.0
54	45	0.25	39.9	326.53	7.05	74	1.6	10.9
13	9	0.40	15.7	362.90	8.33	26	0.6	33.5
67	35	0.15	52.5	329.30	7.54	96	2.3	8.3
72	47	0.15	53.8	232.73	3.91	140	2.4	5.5
53	27	0.14	41.7	585.15	14.22	43	1.1	19.8
44	28	0.42	17.0	26.20	0.80	392	12.3	1.7
51	35	0.27	26.2	116.50	2.40	135	2.8	5.4
39	27	0.15	45.8	745.69	14.25	37	0.7	23.4
46	28	0.15	42.8	1510.82	18.61	17	0.2	68.2
42	32	0.15	42.0	402.26	4.59	63	0.7	13.2
45	31	0.15	43.2	26.44	0.85	988	33.0	0.7
68	52	0.14	44.2	314.67	5.95	85	1.6	9.3
80	54	0.17	42.1	38.22	1.03	665	18.4	1.1
82	60	0.25	23.1	71.81	1.72	194	4.8	3.5
66	49	0.12	24.8	104.28	3.75	672	44.7	4.6
48	31	0.31	31.6	33.88	1.02	562	17.4	1.3
50	30	0.18	38.5	241.50	5.56	96	2.3	8.5
40	27	0.29	33.5	335.63	7.54	60	1.4	15.5
23	17	0.28	44.1	1628.61	22.71	16	0.2	74.8
65	50	0.30	46.6	179.51	3.85	156	3.4	4.8
27	20	0.28	46.4	6353.59	54.62	4	0.04	124.8
54	39	0.25	41.0	755.52	10.17	33	0.4	27.0
68	50	0.09	33.2	2.47	0.53	8126	2236.0	0.1
37	25	0.20	43.4	791.84	8.90	33	0.4	25.8
43	31	0.28	42.0	511.11	8.45	50	0.8	16.3
65	55	0.42	26.7	13.08	0.42	155	5.8	0.7
43	36	0.53	16.0	10.80	0.57	893	49.3	0.8
51	38	0.56	15.9	30.98	0.96	310	9.9	2.2
85	72	0.46	24.2	29.66	0.62	492	10.4	5.2
53	43	0.70	14.8	15.30	0.44	584	17.5	2.9
24	19	0.75	10.1	48.05	1.36	126	3.7	5.6
47	46	1.37	6.9	26.91	0.88	154	5.2	4.2
42	41	0.72	9.9	34.22	0.82	174	4.3	4.0
107	89	0.32	35.9	28.65	0.71	754	19.1	3.1
29	19	0.39	17.3	129.72	3.00	80	1.9	10.7
17	10	0.11	45.6	1463.57	31.17	21	0.4	58.6

promising approach documents that channel-slope variations (or channel-steepness indices) may be an appropriate indicator for erosion, because they are sensitive to a larger range of erosion rates before attaining threshold values (e.g., Whipple, 2004). This inference is supported by studies in which channel slopes continue to steepen when hillslopes have already reached their threshold value (e.g., DiBiase et al., 2010; Ouimet et al., 2009). However, one critical component that remains to be quantitatively assessed through field observations is the interplay of climatic conditions and erosive processes. In addition, the spatiotemporal characteristics of climate variability and its impact on erosion rates are not well known. Numerical modeling studies highlight the impact of runoff intensification, variability, and transience on channel-network behavior (e.g., Lague et al., 2005; Tucker and Slingerland, 1997), but these studies may not readily be transferred into landscape-erosion rates.

In this study, we address this problem and exploit the steep east–west climatic gradient in the high-relief landscape of the southern Central Andes of northwestern Argentina to evaluate the importance of climatic conditions on erosion rates at millennial time scales. In a first step, we analyze catchment-mean erosion rates through cosmogenic nuclide

inventories from varying catchment sizes (~18–25,000 km^2) across the climatic gradient as characterized by calibrated satellite-derived rainfall data (Bookhagen and Burbank, 2010; Bookhagen and Strecker, 2008). These data allow us to quantify climatic and erosional gradients across the Andes and evaluate the impact of climatic conditions on channel slopes. In a second step, we explain the spatial erosion patterns with a straightforward specific stream-power approach. The product of channel slope (derived from a digital elevation model) and discharge (obtained from calibrated satellite-rainfall data) divided by channel width (approximated by a power-law relation with discharge), serves as a first-order explanation of erosion patterns. Specific stream power is similar to the normalized steepness index (k_{sn}) when channel width is scaled by discharge with a power-law exponent of 0.5. However, across the steep climatic gradient of the southern Central Andes, nonlinear relations between drainage area and discharge are pronounced and we emphasize the importance of discharge (i.e., climate) as an erosional forcing factor in this environment. Our specific stream-power/erosion-rate relation is valid on millennial time scales associated with the time scales encapsulated in cosmogenic nuclide erosion rates. Finally, we use the sedimentation history of a landslide-dammed paleolake at the outlet of the Calchaquíes basin in the semi-arid interior of the orogen (Bookhagen et al., 2001; Trauth and Strecker, 1999) as a paleoclimatic archive to document the temporal variability of erosion rates between the pluvial Minchin phase (~30 ka) and the present-day. Our comparison of past and present-day catchment-mean erosion rates documents that climatic conditions have a profound impact on magnitudes of erosion rates in the southern Central Andes and that the threshold landscapes in this region can significantly impact the routing of sediment by increasing runoff during humid periods. Consequently, increased erosion rates during wetter periods may explain some of the discrepancies between erosion records obtained at millennial time scales and beyond (e.g., Kirchner et al., 2001; Thiede et al., 2009).

Taken together, our study points to a strong climatic impact on sediment-transfer rates in this tectonically active mountain range on 10^3 to 10^4-yr time scales. Importantly, our analysis compares erosion rates from similar geologic, but distinctly different environmental conditions to elucidate the impact of climate on the erosional regime. As such, the quantification of erosion rates can be used to enhance our understanding of the behavior of threshold and transient landscapes and to decipher some of the complex interactions between tectonic and climatic feedback processes.

2. Geologic and climatic setting

2.1. Geologic setting

The tectonic evolution and morphology of this region of the southern Central Andes is characterized by Cenozoic basement uplifts, largely related to compressionally reactivated Cretaceous normal faults (Grier et al., 1991; Mon and Salfity, 1995) and Paleozoic structural fabrics (Hongn and Hippertt, 2001). Some of these uplifts still have former rift-related sedimentary and volcanic rocks in their hanging walls (Mon and Salfity, 1995; Viramonte et al., 1999). The basement uplifts created several intermontane basins between the eastern margin of the arid Altiplano–Puna Plateau in the orogen interior and the humid undeformed Andean foreland that were repeatedly filled and excavated during the Plio-Pleistocene (Bossi et al., 2001; Carrapa et al., 2008; Hain et al., 2011; Hilley and Strecker, 2005; Mortimer et al., 2007; Strecker et al., 2007). The uplifted basement blocks constituting the eastern margin of the internally drained Altiplano–Puna Plateau primarily consist of Paleozoic amphibolites and migmatites together with plutonic and pegmatitic rocks, while the ranges in the broken foreland are mainly comprised of late Proterozoic greenschist-facies metasedimentray rocks and granites (Mon and Hongn, 1991; Mon and Salfity, 1995; Ramos, 2008).

The quartz content of these rock types varies and thus sample locations of smaller catchments were chosen to reflect single lithologies, because variations of quartz content can bias calculated catchment-mean erosion rates derived from cosmogenic nuclide inventories (Bierman and Steig, 1996). Rock fracturing and differences in material strength between lithologies may influence slope stability thresholds and thus topographic metrics (e.g., hillslope angle and relief) (Molnar et al., 2007). Nonetheless, the geologic evolution of this region indicates a similar tectonic character, and we have not observed large variations in rock-strength parameters throughout the study area.

2.2. Climatic setting

South America experiences a highly seasonal climate (e.g., Grimm et al., 2005; Rao et al., 1996; Vera et al., 2006; Zhou and Lau, 1998). During the austral summer, an anomalous wind flow from the sub-Saharan region enhances the tropical North Atlantic trades and water-vapor transport onto the South American continent (e.g., Vera et al., 2006). There, the developing South American low-level jet transports North Atlantic and recycled moisture from the Amazon basin along the eastern Andean flanks southward (Eltahir and Bras, 1994; Vera et al., 2006). Along the eastern Andean flank, wet air masses interact with steep topography and orographic rainfall results in pronounced climatic gradients with progressively drier conditions toward the Altiplano–Puna Plateau (Bookhagen and Strecker, 2008; Schwerdtfeger, 1976). Water-vapor transport toward the orogen interior is controlled by the locations of the Chaco Low and the Northwestern Argentinean Low, which in turn control the position of the low-level jet (Cook and Vizy, 2006; Marengo et al., 2004; Seluchi et al., 2003; Vera et al., 2006; Vizy and Cook, 2007).

Various geologic archives document the impact of this climate system. For example, during the pluvial Minchin phase (~25–40 ka), water-vapor transport toward the orogen resulted in lake highstands in the southern Central Andes (Bookhagen et al., 2001; Trauth et al., 2003) and on the Altiplano-Puna Plateau (e.g., Abbott et al., 2003; Baker et al., 2001; Markgraf and Seltzer, 2001; Placzek et al., 2006; Seltzer et al., 2003). In addition, multiple moraine generations in the high-elevation, semi-arid highlands of the Eastern Cordillera of Argentina and Bolivia (e.g., Haselton et al., 2002) suggest that water-vapor transport and hence precipitation in these highlands has greatly varied at glacial–interglacial timescales. The impact of protracted millennial-scale climate changes on mass transport has also been documented in this environment by clusters of deep-seated bedrock landslides during late Pleistocene and Holocene wet periods (Hermanns and Schellenberger, 2008; Hermanns et al., 2000; Trauth et al., 2000). The greater availability of moisture in these environments during the past is furthermore suggested by paleoclimate modeling (Cook and Vizy, 2006).

3. Methods and data

3.1. Cosmogenic nuclide erosion rates

Present-day river sediments were collected from active channels in 41 catchments ranging in size from 18 to approximately 24,500 km^2, and with mean elevations between 0.82 and 4.12 km asl (Table 1, Fig. 1, Figure DR1) to determine catchment-mean erosion rates (e.g., Granger et al., 1996; von Blanckenburg, 2005). Catchment-mean erosion rates were determined using standard analytical procedures from concentrations of in situ produced ^{10}Be in quartz from alluvial sediments. We have streamlined previous processing methods (e.g., Kohl and Nishiizumi, 1992; von Blanckenburg et al., 2004) and provide a constantly updated, detailed, step-by-step manual at http://www.geog.ucsb.edu/~bodo/pdf/bookhagen_chemSeparation_UCSB.pdf. In short, we cleaned the 0.25–0.5 mm river-sand size fraction through magnetic and heavy-liquid separations followed by a 12-hour bath in a 1:1

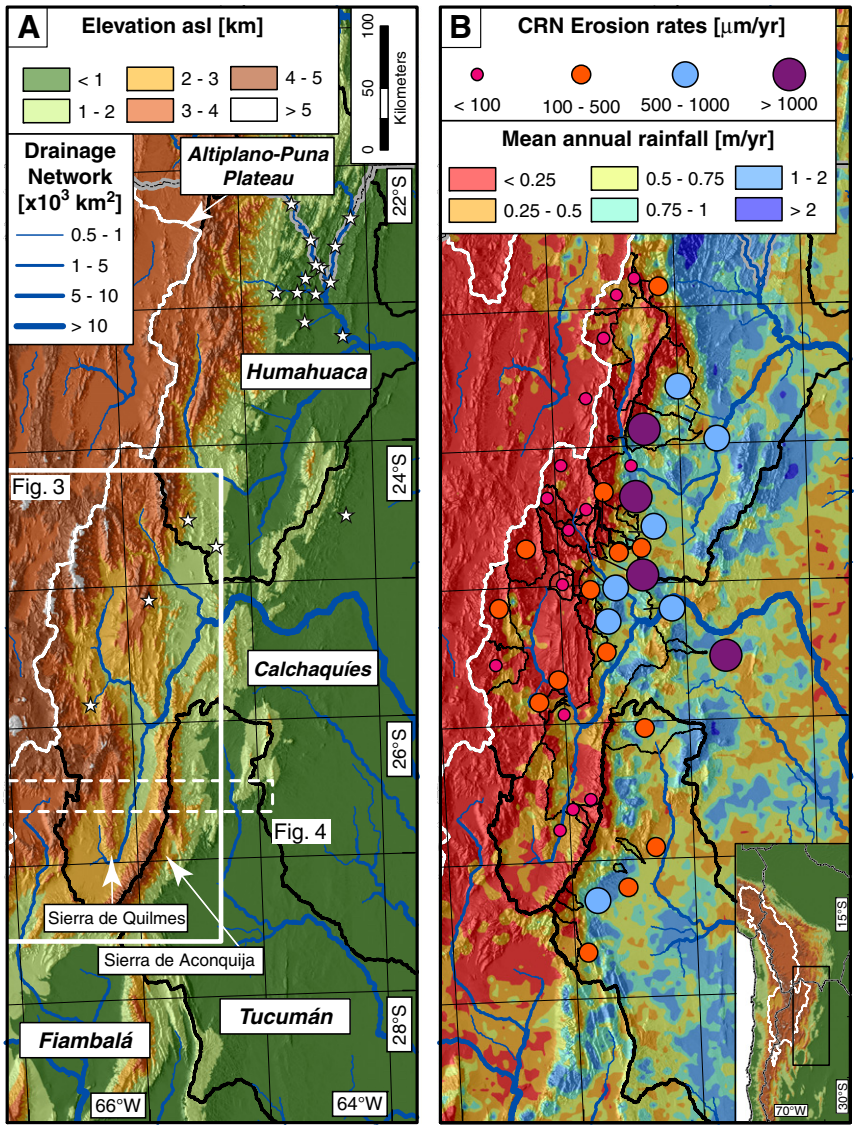

Fig. 1. Topographic overview of study area. (A) denotes major catchment boundaries in black and the eastern part of the internally-drained Altiplano–Puna Plateau, outlined in white (see inset in B for large-scale geographic setting). Stars mark locations of discharge sites used for validating remotely-sensed rainfall data (cf. Fig. 2). Rectangular white box shows area of the Calchaquíes Basin, which integrates drainage from the Santa María and Calchaquíes rivers (Fig. 3) and dashed white polygon outlines swath-profile area (Fig. 4). (B) shows a compilation of all cosmogenic-nuclide catchment-mean erosion rates with color and size of circles scaled to erosion-rate magnitude (in μm/yr). Mean annual rainfall amounts are derived from calibrated TRMM2B31 (Bookhagen and Strecker, 2008). See Table 1 for more detailed information. Note that generally steep and wet catchments on the eastern Andean margin have higher erosion rates than catchments in the climatic transition zone with the internally drained Altiplano-Puna.

hydrochloric acid solution. Next, samples were leached at least three times in a 2% hydrofluoric acid solution to remove all non-quartz minerals and meteoric beryllium in an ultrasonic bath or on a commercial hot-dog roller. Our cleaned samples weighed between ~80 and ~120 g. They were dissolved in hydrofluoric acid and, after addition of a low-ratio ^{9}Be spike (10/9Be ratio of ~1×10^{-15}), beryllium and aluminum separated by ion-exchange chromatography. Subsequently, accelerator mass spectrometry (AMS) measurements were carried out at Lawrence Livermore National Laboratory. We rely on the original ICN standard (Nishiizumi et al., 2007) as reference and use a value of 5.1×0^{-7} yr^{-1} as decay constant for ^{10}Be. Production rates were calculated for every 250-m pixel, including variations in altitude, latitude, spallation and muon production, and topographic shielding. Muonogenic production rate calculations are based on formulations and constants described in Granger and Muzikar (2001). We do not find significant differences (<5%) compared to the scaling procedure described by Schaller et al. (2001). Sea-level, high-latitude (SLHL) spallogenic production rate is 4.7 atoms g^{-1} yr^{-1} (Balco et al., 2009). At present, there is no seasonal or permanent snow or ice cover in this part of the Andes, and thus we did not correct for snow shielding. Table 1 lists the production and catchment-mean erosion rates, calculated ^{10}Be concentrations, their corresponding 1-σ errors, and catchment-associated geomorphic parameters. We only included errors associated with AMS measurements; including errors from production-rate uncertainties will increase errors on average by 15%, but will not change data interpretation.

3.2. Satellite-derived rainfall

We characterize the climate of the region with calibrated remote-sensing data derived from the TRMM (Tropical Rainfall Measurement Mission) platform using product 2B31. In this approach we follow the methods described in Bookhagen and Strecker (2008) and Bookhagen and Burbank (2010) and extended data calibration to 13 years from 1998 to 2010. The data have a spatial resolution of 5×5 km^2 and record the steep orographic rainfall gradient across the eastern Andes (Bookhagen and Strecker, 2008). We use these data to route mean

annual rainfall to create mean annual discharges with a simple D8 routing scheme where all water flows along its steepest path. We do not account for evapotranspiration, seasonal snowmelt, and groundwater loss. Particularly evapotranspiration is likely to impact runoff in this region (e.g., Mu et al., 2007). Despite our simplified approach, we accurately capture the mean annual discharge gradient, although our data overpredict discharge by a factor of 1.4 ± 0.1 (Fig. 2). Using the same routing scheme for the more widely used TRMM 3B42, a gridded data product with a spatial resolution of $\sim 30 \times 30$ km^2 (Huffman et al., 2007), results in an overprediction of gauged discharge by a factor of 1.1 ± 0.1 (Fig. 2, 2 Figure DR2). These coarser data, however, do not capture the orographic rainfall gradient in this area (Figure DR3) and TRMM3B42 rainfall data were adjusted with discharge measurements. We note that the actual flow routing of rainfall for each grid cell is different than multiplying the drainage area with rainfall to estimate discharges (Figure DR4 and DR5) (Anderson, 1994).

3.3. Specific stream power (SSP) and topographic analysis

We use specific stream power as a proxy for spatial variation in erosion. The concept of stream power was first introduced by Bagnold (1960) and defined in terms of the power per unit area of stream bed (shear stress multiplied by flow velocity). We note that Gilbert (1877) used a similar concept called capacity. Stream power provides an expression of the rate of energy expenditure at a given point in a river system and is inherently linked to sediment-transport competence. Earlier work highlights the validity of this approach to describe bed-load transport and erosion in rivers (e.g., Anderson, 1994; Bagnold, 1977; Knighton, 1999). The total stream power is:

$$\Omega = \gamma \cdot Q \cdot S. \tag{1}$$

Where Ω is total stream power per unit length of channel (W m^{-1}) and γ is the specific weight of water (~9810 N m^{-3}), Q is the water discharge (m^3 s^{-1}), S the energy slope approximated by the bed slope (m m^{-1}). Several studies have shown that the use of specific stream power (SSP) may by more suitable than total stream power channel-process. Specific stream power is expressed as ω (W m^{-2}):

$$\omega = \frac{\gamma \cdot Q \cdot S}{w} = \frac{\Omega}{w} \tag{2}$$

where w is the river width (m). Unit stream power is related to the mean boundary shear stress (τ, N m^{-2}) multiplied by the mean flow velocity ($\bar{u}$, m s^{-1}).

We calculated SSP for every 90-m grid-cell point, where discharge was taken from the calibrated TRMM data, channel slopes were derived from the Shuttle Radar Topographic Mission Digital Elevation Model (SRTM DEM) (Farr et al., 2007), and river width was scaled with discharge using a power-law exponent of 0.4 (e.g., Craddock et al., 2007; Knighton, 1999; Whipple, 2004). Previous studies calculating specific stream power along river profiles in the Himalaya have relied on a channel-width scaling including a slope factor (Finnegan et al., 2005). We have performed our calculation using this approach and do not observe significant differences in the results; hence, we apply the simple power-law scaling. We calculate channel slopes only along the fluvial network by fitting a line to the previous and following five elevation values, resulting in an average of 11 pixels. We remove slope values with a low or negative coefficient of correlation (~0.1% of the data). We note that channel slopes extracted from the SRTM DEM have similar relative magnitudes and spatial distribution as channel slopes derived from the ASTER GDEM [http://www.gdem.aster.ersdac.or.jp/index.jsp]. SSP was calculated for all drainage areas >1 km^2. In order to visualize the spatial SSP distribution and to create a continuous surface, we applied a 5-km smoothing window with an exponential distance weighting (Fig. 3). All calculations and correlations between cosmogenic nuclide erosion rates are based on the non-interpolated raw data; hence, the interpolation is purely intended for visualization. SSP with a scaling relation of 0.5 between discharge and river width mimics the spatial distribution of the normalized steepness index (k_{sn}) (cf. Figure DR6) (Kirby et al., 2003; Wobus et al., 2006).

In order to calculate paleo-erosion rates for the Calchaquíes basin, we take advantage of earlier work (Trauth et al., 2003) combined with new DEM constraints and our own field surveys and observations. We estimate the sediment volume associated with a late Pleistocene (~30 ka) landslide that impounded the outlet of the Calchaquí basin and resulted in an extensive paleolake (Bookhagen et al., 2001; Hermanns et al., 2000; Trauth et al., 2000). Pre-landslide topography

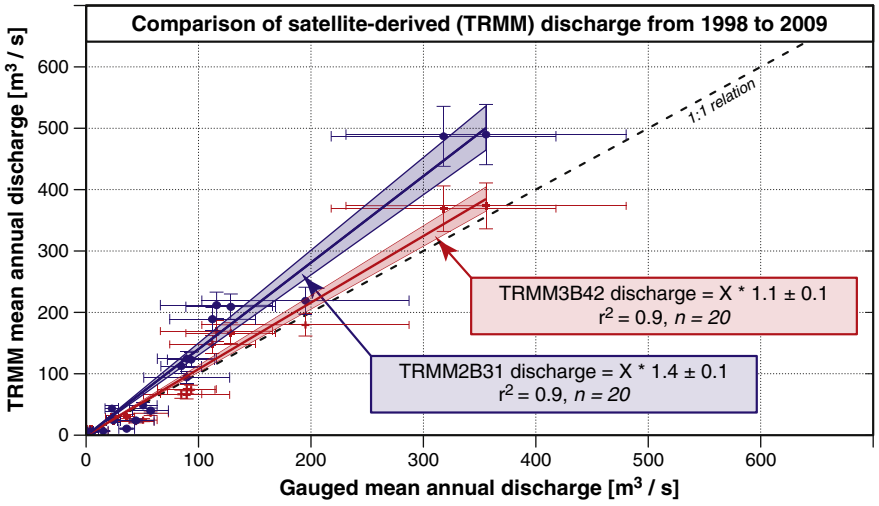

Fig. 2. Comparison of remotely sensed rainfall data with 20 gauge measurements from NW Argentina (see Fig. 1 for station location). In this study, we rely on the Tropical Rainfall Measurement Mission (TRMM) product 2B31 data (Bookhagen and Strecker, 2008) with a $\sim 5 \times 5$ km^2 spatial resolution that captures the overall discharge gradient, but overpredicts gauged discharges by a factor of ~1.4 (~1.1 for the coarser and discharge-corrected $\sim 30 \times 30$ km^2 TRMM 3B42 data). This discrepancy is related to the high evapotranspiration in the arid intermontane basins and does not impact relative contributions. Error bars indicate 1-σ standard deviation of the 12-year mean annual records.

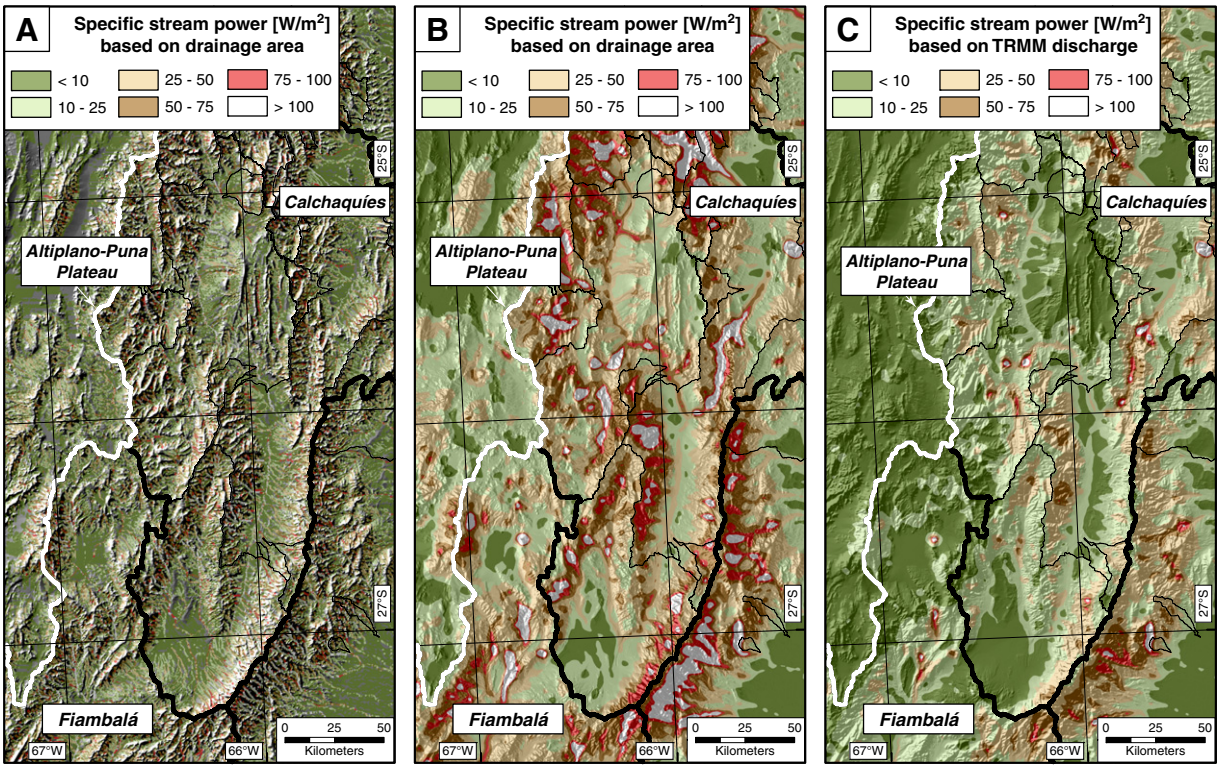

Fig. 3. Calchaquíes drainage basin (see Fig. 1 for location) and representation of spatially continuous specific stream power data. Bold white line delineates the Altiplano–Puna Plateau drainage divide, bold black line indicates the combined catchment area of the Santa María and Calchaquíes rivers that constitute the Calchaquíes drainage basin. Thin black lines outline sampled basins. (A) Specific stream power for each grid point (90×90 m^2) with a drainage area >1 km^2. The non-continuous data has been interpolated with a 5-km distance weighted smoothing window to create a continuous surface shown in (B). In both cases, specific stream power is calculated according to Eq. (2) and is based on drainage area as discharge proxy. (C) Specific stream-power calculations based on satellite-derived (TRMM) discharge used in this study.

and stream gradients were reconstructed by removing landslide deposits from the DEM and connecting upstream and downstream channel sections by an equilibrium river profile. We assume that sedimentation rates of landslide-dammed lakes represent upstream denudation rates, because all fluvially transported material was retained in the lake basin.

4. Results

4.1. Climatic gradients and cosmogenic nuclide erosion rates

Our cosmogenic nuclide catchment-mean erosion rates show an east–west gradient, with generally higher erosion rates at the wet, eastern Andean flanks and decreasing values westward toward the arid orogen interior (Fig. 1B). A characteristic E–W swath profile across the orogen encompassing the south-central part of the Calchaquíes basin and combining several locations for which cosmogenic nuclide measurements were obtained, clearly reveals the erosional gradient and the strong relationship with mean annual rainfall (Fig. 4A). In the easternmost humid, gently sloping foreland areas erosion rates are moderate at 0.13 ± 0.004 ($n=1$) mm/yr. Erosion rates increase to 0.50 ± 0.3 mm/yr ($n=15$) at the steep east-facing orographic barriers, where mean annual rainfall rates are up to 2 m/yr. In contrast, on the western, dry slopes of the ~5-km-high Sierra Aconquija about 25 km to the west, erosion rates are one order of magnitude lower (0.05 ± 0.02 mm/yr, $n=4$), despite similar lithologies and slopes. Erosion rates within the even more arid intermontane basins along the eastern flank of the Altiplano–Puna Plateau remain low, but slightly increase by a factor of two to 0.1 ± 0.04 mm/yr ($n=4$) at the next orographic barrier to the west with mean annual rainfall amounts of 0.5 m/yr. Erosion rates of basins immediately to the east of the Altiplano–Puna Plateau drainage divide are similar (0.02 ± 0.01 mm/yr, $n=5$) to erosion rates on the internally drained plateau (0.02 ± 0.0004 mm/yr, $n=1$). We have omitted sample STR-22 in the Humahuaca Basin taken in an active alluvial fan with unstable channel walls that shows an erosion rate of 8.1 mm/yr. Catchment-mean erosion rates average over <1 to ~50 ka with an *e*-folding depth of 60 cm ($160\ \mathrm{g\ cm^{-2}}/2.65\ \mathrm{g\ cm^{-3}}\approx60$ cm).

4.2. Climatic gradients and specific stream power (SSP) variations

Along the same swath profile as discussed above (cf. Fig. 1A, Fig. 4B), we show the variation of SSP calculations based on discharge scaled with drainage area (SSP0) and discharge derived from TRMM rainfall (SSPT). In the wet, eastern parts, both approaches of determining stream power are similar. However, once the first orographic barrier is crossed, SSP calculated from the corresponding drainage area remains high (and even increases), while SSPT decreases towards the Altiplano–Puna Plateau and follows the decreasing trend in erosion rates (Fig. 4B). In the arid intermontane basins, SSP0 overpredicts stream power by a factor of 2 to 6. At the scale of the NW Argentine Andes, our satellite-derived rainfall and discharge analysis indicates that the rainfall gradient has significant impact on the spatial distribution of specific stream power (Fig. 5, DR7), normalized steepness index (Figure DR8), and the general trend in erosion rates.

4.3. Paleo-erosion rates

We have estimated the late Pleistocene sediment volume stored during the existence of the large paleolake in the Calchaquíes basin to be 72.6 km^3. The sediment was deposited within 6700 yrs behind a landslide dam in the upper Quebrada de las Conchas, east of the confluence of the Santa María and Calchaquíes rivers (Bookhagen et al., 2001; Trauth et al., 2003). Our calculations reveal an averaged

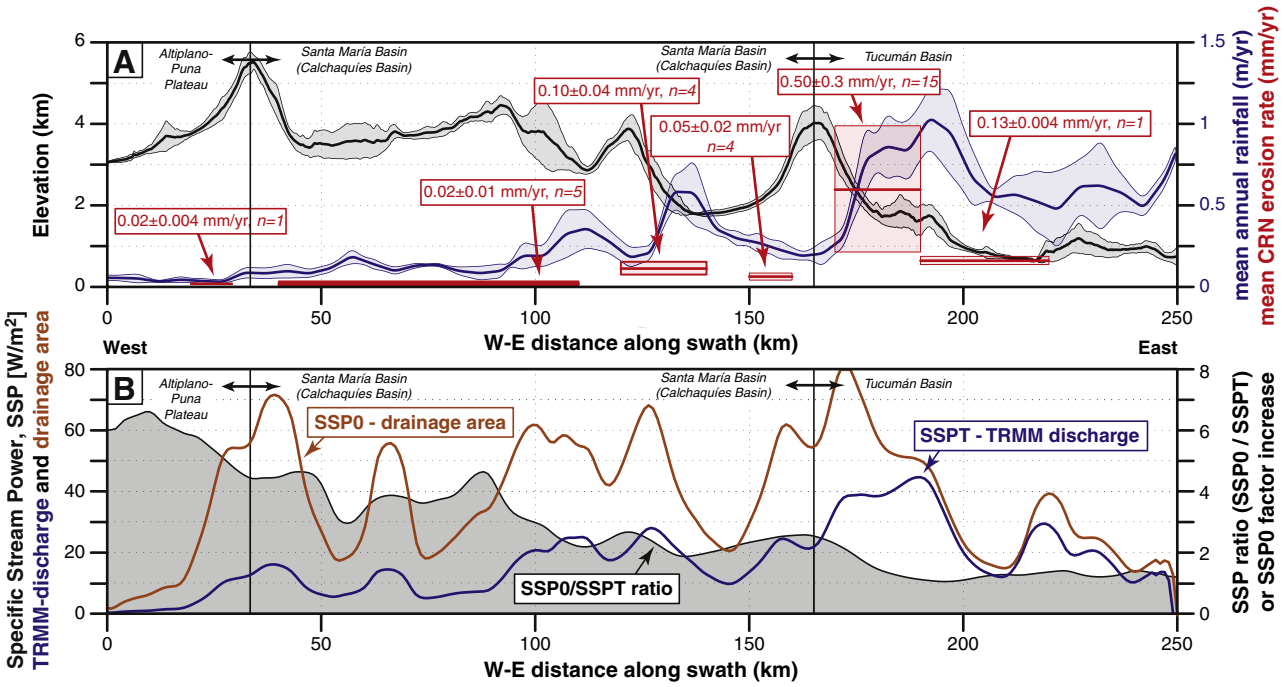

Fig. 4. Topography, rainfall, and cosmogenic radionuclide erosion rate (A) and comparison of specific stream-power (SSP) models (B) within a 50-km-wide west-to-east swath across the central Santa María Basin (Calchaquíes Valley, see Fig. 1 for swath location). The Sierra Aconquija constitutes the divide between the Santa María and Tucumán basins and is the eastern orographic rainfall barrier. (A) Heavy black line indicates mean topography and gray shading denotes $\pm 1\sigma$ values; heavy blue line indicates mean annual rainfall from calibrated TRMM 2B31 data with 1σ variation (blue shading). We have synthesized catchment-mean erosion rates for the wet, dry, and internally drained catchments for the Humahuaca, Calchaquíes and Tucumán basins (cf. Fig. 1B) with sizes from 4 to 100 km^2 and omitted larger catchments spanning basins with more than one orographic barrier. Erosion rates from samples collected in the easternmost sectors of the study are based on sample STR-4, the first orographic barrier combines 15 samples (STR-1, -5, -6, -17, -25, -26, C6, AFL, PORT, WIE, CALD, VAQU, ARG-11, -12, -13); the erosion rates on the western, dry flank of the first orographic barrier are based on 4 samples (STR-3, -9, -10, C3), erosion rates at the next moderately elevated orographic barrier were derived from 4 samples (STR-2, -11, -13, -19); erosion rates on the eastern flank of the Altiplano–Puna drainage divide are based on 5 samples (STR-14, -8, -23, C1, C2), and the single erosion-rate measurement from the eastern Altiplano–Puna Plateau is from sample STR-18. Note the westward decrease in erosion rates: compared to the humid sectors of the transect the dry, western basins bordering the Altiplano-Puna Plateau have significantly lower erosion rates, despite similar channel steepness. (B) Comparison of TRMM-discharge (blue line) and drainage area (orange line) derived SSP and their ratio (black line with gray polygon). The factor of SSP overprediction increases from East (right) to West (left), with highest values near the border of the Altiplano–Puna Plateau.

sedimentation rate of 0.5 ± 0.1 mm/yr. This value represents a minimum for catchment-mean erosion rates during the late Pleistocene as the calculated sediment volume mostly consists of silty lake sediments and does not include bedload deposits along the paleo rivers.

5. Discussion

Our 41 new cosmogenic nuclide data show a westward-decreasing trend in erosion rate across the Andean orogen spanning the humid eastern flanks and the arid Altiplano–Puna Plateau (Fig. 1, Fig. 4). A similarly steep, tenfold rainfall gradient from the humid foreland to the arid orogen interior derived from more than a decade of calibrated, high-resolution satellite data suggests a strong climatic impact on erosion rates. These conditions make the southern Central Andes an ideal setting to test the impact of climatic gradients on catchment-mean erosion rates. In particular, ubiquitous lithologies rich in quartz (e.g., Mon and Salfity, 1995), large drainage basins (>50 km^2), and uniform vegetation and rainfall regimes within the different climatic compartments lend themselves to an integral analysis of climate conditions and erosion. The size of the basins minimizes an impact of late Pleistocene landslides (e.g., Bookhagen et al., 2001; Hermanns et al., 2000; Trauth et al., 2000) on cosmogenic nuclide-derived catchment-mean erosion rates (Niemi et al., 2005). Before analyzing the data in the context of topographic and climatic metrics, we assess the robustness of the data.

First, we have tested the consistency of sediment mixing from areas with different erosion rates by calculating differential erosion rates following Granger et al. (1996). We accordingly assume that different areas contribute sediment in proportion to their erosion rates when averaged over long time scales. Sample M1 with an erosion rate of 0.65 mm/yr was collected in the Rio Juramento, downstream from the outlet of the Valles Calchaquíes. We have taken four large sub-catchments (samples M2, M3, C4, C6) and have calculated the differential erosion rates for the downstream section of the Rio Juramento to 0.72 ± 0.1 mm/yr (Fig. 6). We subsequently compared this value to a catchment in the same environment (Rio Escoípe, sample STR-6) that provided an erosion rate of 0.67 ± 0.05 mm/yr. This catchment is located in the downstream portion of the Calchquí basin (M1) and the STR-6 erosion rate is very similar to the predicted differential erosion rate. Corresponding calculations for smaller catchment areas, for example in the sub-basins of the northern Santa María Basin, provide equally well-matching values. This consistency leads us to suggest a generally robust erosion-rate dataset that comprises our well-mixed river-sand samples.

Second, our erosion rates average over time scales of up to ~50 ka and thus take into account several humid phases (e.g., Placzek et al., 2006). Studies in the northern Central Andes of Bolivia suggest that erosion rates may be biased in a landscape not in cosmogenic-nuclide equilibrium (Insel et al., 2010). Numerical modeling has demonstrated that erosion rates derived from cosmogenic nuclides deviate strongly from true erosion rates in environments with long climatic oscillations and high erosion rates (Schaller and Ehlers, 2006). The intermontane basins straddling the eastern Altiplano–Puna Plateau have been characterized by pronounced, short-term climatic changes. In these basins, erosion rates are generally low, but increased over time scales of a few thousand years, as indicated by paleo-climatic reconstructions (e.g., Bookhagen et al., 2001; Markgraf and Seltzer, 2001; Seltzer et al., 2003; Trauth et al., 2003). We suggest that our present-day

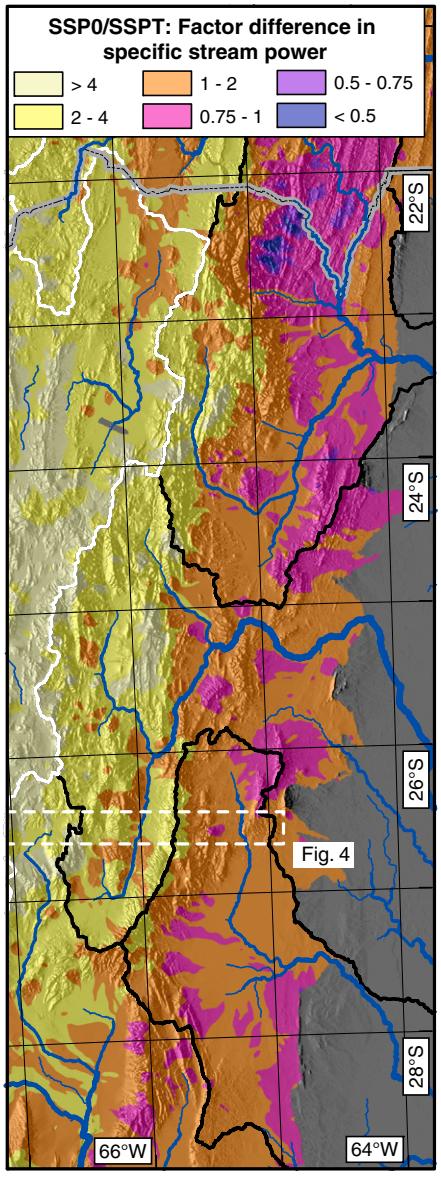

Fig. 5. Difference between specific stream power (SSP) calculated with drainage area (SSP0) as proxy for discharge and TRMM-derived discharge (SSPT). Differences are shown as the ratio of SSP0/SSPT; values larger than 1 denote areas where SSP0 is larger than SSPT and vice versa. For example, the arid basins bordering the Altiplano–Puna Plateau (bounded by white line) have 2 to >4 times higher SSP0 than SSPT. The opposite relationship is true for the humid, east-facing slopes at the first orographic barrier. Note that we have applied the same 5-km-smoothing window for both SSP calculations to visualize a continuous surface; all calculations were performed on channels with a drainage area >1 km^2 using Eq. (2) and limited to mountainous catchments with elevations >500 m asl. White-dashed rectangular polygon outlines swath shown in Fig. 4.

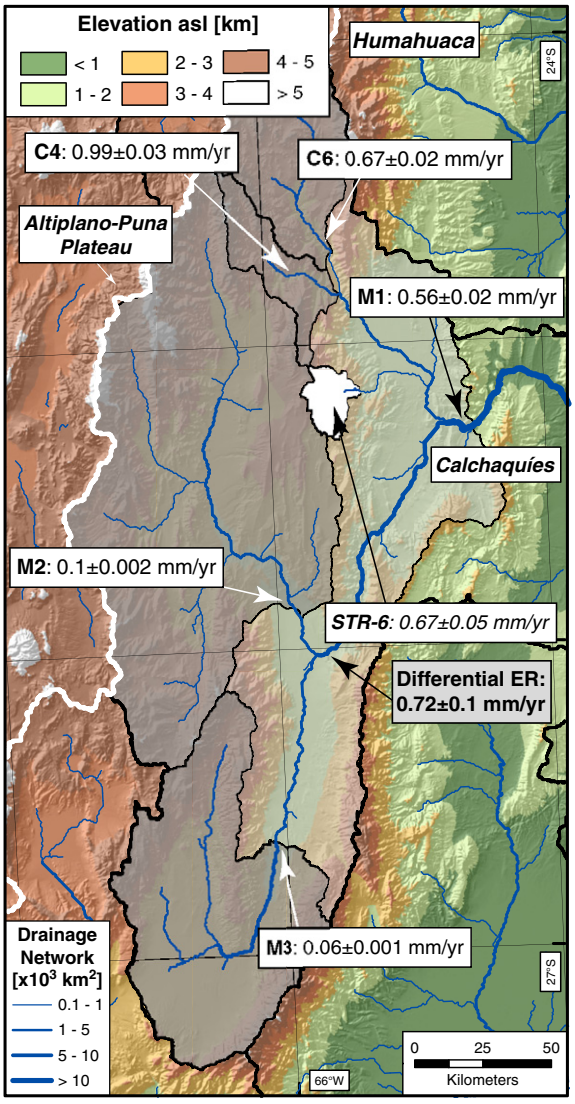

Fig. 6. Results of sediment mixing and differential erosion-rate calculation for the Calchaquíes valley. Four samples (C6, C4, M2, M3) constitute sub-catchments of the Rio Juramento sample M1, which was taken near the outlet of the Calchaquíes Valley. The differential erosion rate (ER) 0.72 ± 0.1 mm/yr takes into account the areally weighted ER from each sub-catchment (Granger et al., 1996). The sample STR-6 (ER: 0.67 ± 0.05 mm/yr) is located within this differential erosion-rate area and is used for a comparison with the calculated differential erosion rate. The consistency of the data and overlap within 1-σ error bars supports the assumption of well-mixed river-sand samples.

catchment-mean erosion rates reflect true erosion rates and are not significantly biased by climatic oscillations.

5.1. Climatic impact on channel slopes in threshold environments

In order to investigate the threshold behavior of hillslopes, we have divided the study region into 2 to 20 km^2 catchments (Figure DR9). For each catchment (n = 24′197) we derived the mean and 1-σ standard deviation of the normalized steepness index, hillslopes angle, and mean annual rainfall amounts (Fig. 7). We distinguish between arid (<0.25 m/yr annual rainfall, n = 7185 catchments), moderate (0.25<x<0.75 m/yr, n = 9497) and humid (>0.75 m/yr, n = 7515) areas. For each of the rainfall compartments, we observed a slightly different relationship, but each demonstrates that normalized steepness values in wetter areas generally result in steeper mean hillslope angles (Fig. 7). This relationship is nonlinear and most pronounced at steepness values between 100 and 200, where hillslopes in humid catchments are 2 to 3° steeper than arid catchments (see inset in Fig. 7). This likely reflects the more frequently occurring hillslope-transport processes (i.e., landslides, debris flows) in the humid areas that result in overall steeper 2–20 km^2 catchments.

We further investigate this slight, but important discrepancy by analyzing drainage area, discharge, and channel-slope variations (Fig. 8). An interesting pattern emerges indicating that with the same drainage area (or distance from the drainage divide), wetter regions have lower channel slopes than dry areas (with moderate regions in between). This finding is not surprising, as the energy balance of a river as given in Eq. (2) depends on discharge and slope. Consequently, for similar channel widths, drier channels with

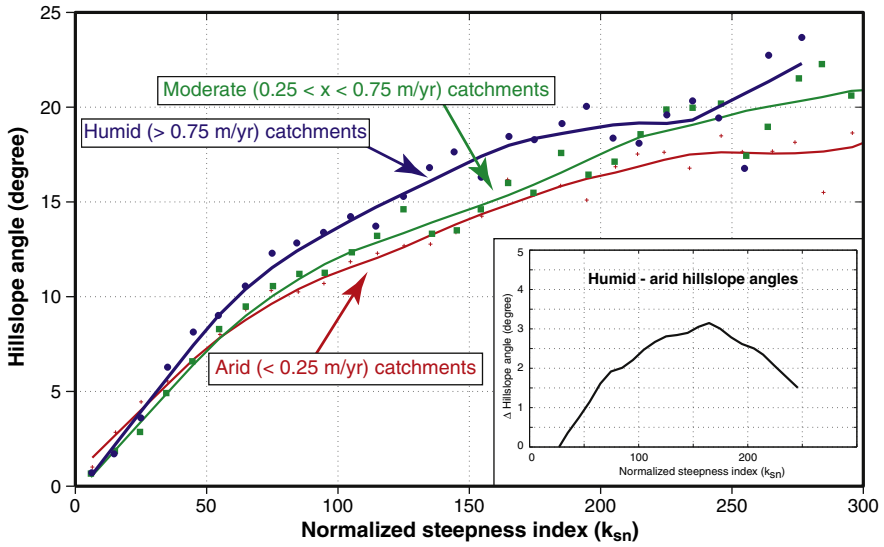

Fig. 7. Relation between normalized steepness index and hillslope angle for arid (red crosses), moderate (green squares), and humid (blue circles) catchments in northwestern Argentina. A total of 24′197 2–20 km^2 catchments were analyzed, and a 10-step binning for normalized steepness indices was used (Figure DR9). Solid lines are moving averages. Inset shows the difference in hillslope angle between humid and arid catchments, indicating a 2 to 3 degree difference at moderate normalized steepness values. We note that the relationship for very low and high steepness values is weakly defined due to few data points and we have removed these parts from the inset.

lower discharge must be steeper in order to result in a similar erosion rate. The generally parallel, but offset power-law relations in Fig. 8A overlap within their 95% confidence intervals when using satellite-derived discharge instead of drainage area (Fig. 8B).

We emphasize the significance of these observations with respect to the interpretations of normalized steepness indices in tectonically active regions. Our observations suggest that part of the shift or offset in channel slopes between adjacent regions can be explained by climatic, instead of tectonic-uplift gradients. Most tectonically active regions also exhibit steep climatic gradients, and may thus complicate the interpretation of channel-slope variations. Generally, we observe that areas with >0.75 m/yr rainfall exhibit a statistically significant difference in channel-slope characteristics; however, this finding does not take into account the impact of lithology, rock fracturing, and other factors on channel-slope behavior. In this respect, a potentially important parameter is channel width (e.g., Whittaker et al., 2007; Yanites and Tucker, 2010) that has been neglected in this study.

5.2. Erosion rates and topographic metrics

In light of recent attempts to quantify the relation between topometrics with cosmogenic-nuclide derived catchment-mean erosion rates (e.g., Binnie et al., 2007; Cyr et al., 2010; DiBiase et al., 2010; Ouimet et al., 2009), we compare our erosion rates to mean specific stream power values for each sampled basin. Previous studies have related channel-slope measurements (e.g., local slope, specific stream power or normalized steepness index) to erosion rate in the form of slope~erosion rate^p (e.g., Lague et al., 2005; Sklar and Dietrich, 2004; Snyder et al., 2003). Earlier estimates for the power-law exponent p range from $p=1$ (e.g., Kirby and Whipple, 2001; Lague and Davy, 2003), $p=0.5$ (DiBiase et al., 2010; Ouimet et al., 2009), to $p=0.25$ (Snyder et al., 2003). We have fitted a power law to our data that suggests a power-law exponent of $p=0.7\pm0.2$ ($r^2=0.6$) in the above mentioned framework (Fig. 9). We note that our specific stream-power data is based on TRMM2B31-weighted discharge; drainage-area weighted discharges result in higher SSP amounts with a similar power-law exponent but with larger uncertainties of $p=0.7\pm1$ ($r^2=0.4$). A similar relationship emerges for the normalized steepness index, where the power-law exponent for the TRMM2B31-weighted discharge is $p=0.7\pm0.3$ ($r^2=0.6$) and for drainage-area is $p=1\pm1$ ($r^2=0.3$) (Figure DR10).

Other studies have highlighted the link between topometrics and erosion rates (e.g., Binnie et al., 2007; Cyr et al., 2010; DiBiase et al., 2010; Kirby and Whipple, 2001; Ouimet et al., 2009). We build upon these results and exploit the steep rainfall gradient in our study area to highlight the climatic impact on erosion rates. We have analyzed the impact of mean annual rainfall on the CRN erosion rates and observe that arid catchments (<0.25 m/yr) tend to result in higher specific stream power values when discharge is based on drainage area (Figure DR 11). Furthermore, the data indicate that specific stream power values for arid catchments fall into a narrow range, while erosion rates vary by two orders of magnitude (Figure DR 11). We relate TRMM2B31-discharge weighted specific stream power with cosmogenic-nuclide derived erosion rates and observe a robust relation ($r^2=0.7$) below 0.2 mm/yr erosion rates (Fig. 9). Higher erosion rates are not reflected by higher specific stream-power values. The high erosion rates are measured in humid catchments (Table 1, Figure DR 11) and in catchments that have been actively incised where transiently stored sediments are associated with landslides (Bookhagen et al., 2001; Hermanns et al., 2000). Also, erosion rates >0.2 mm/yr have been documented to exceed soil-production rates in similar environments (e.g., DiBiase et al., 2010; Heimsath et al., 1997). Because width in the calculation of specific stream power relies on discharge, our predicted channel width differs between the TRMM2B31-derived and drainage-area based data. For the drainage-area based approach, channels in the semi-arid regions are predicted to be ~1.3 to 2 times wider than satellite-derived discharge channels, while channels in the humid areas are ~0.7 times as wide (Figure DR12).

Overall we record a ten-fold erosion-rate difference along an east to west transect through the southern Central Andes, which appears to be related to the pronounced climatic gradient in that region. Accordingly, we suggest that most changes in the discharge-weighted topographic metrics (either specific stream power or normalized steepness index) are due to the pronounced climatic differences (cf. Fig. 1B, 4). We exclude a major influence of lithologic variability in controlling the measured erosion rates. The lithologic conditions in the east–west transect particularly across the southern sector of our study area are remarkably similar and comprise granites or gneisses, often intruded by granites. The role of variable tectonism, however,

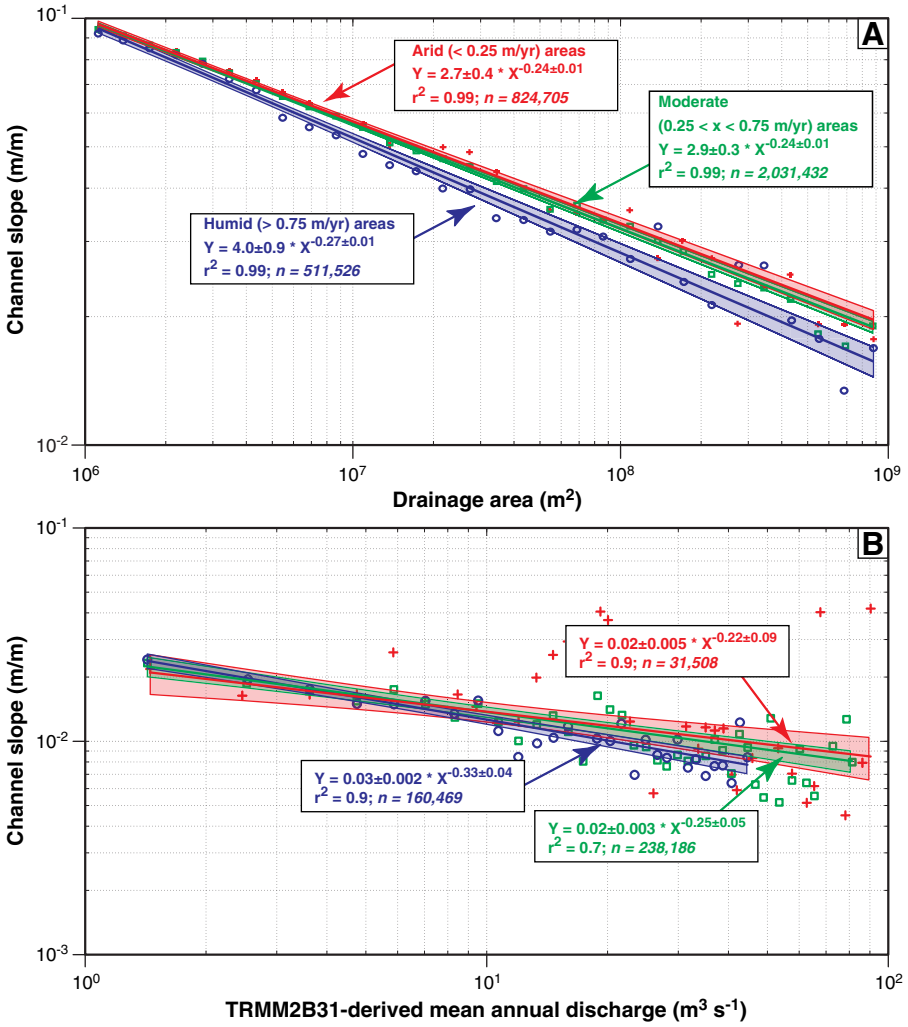

Fig. 8. Comparison of channel slopes vs. drainage area and satellite-derived discharge. (A) shows that humid areas (mean annual rainfall >0.75 m/yr, blue line) have lower channel slopes than arid areas (<0.25 m/yr, red line), whereas moderately humid areas lie in between (green line). We rely on all pixels within the study area (cf. Fig. 1) and show mean log-binned data (number of humid pixels: 824′704, moderate: 2′031′432, arid: 824′705). Shading denotes 95% confidence interval of power-law fits. (B) same plot, but for calibrated satellite-derived mean annual discharge. Note the generally overlapping power-law exponents within their 95% confidence intervals when using discharge instead of drainage area. The slightly larger scatter in the data is likely related to some transient landscape behavior. We ignore potential channel-width changes in this context.

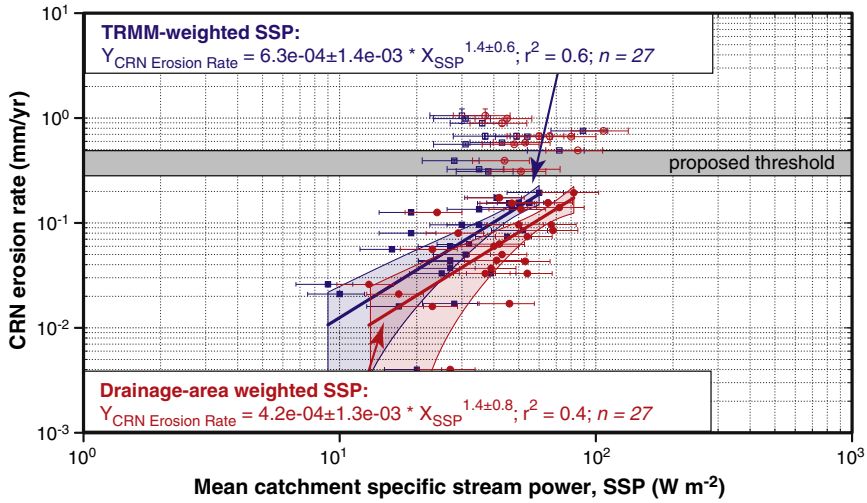

Fig. 9. Relation between mean catchment specific stream power (SSP) and CRN-derived catchment-mean erosion rate. The TRMM-weighted SSP produces a reasonable fit for the data and suggests a power law exponent of ~1.4 (or erosion rate to the power of ~0.7). Only the filled symbols were used for the error-weighted fits (n = 27).

is more difficult to evaluate. There is not enough quantitative data available yet that would allow for an assessment of differences in exhumation rates on timescales comparable to our erosion-rate analysis. However, except for the Sierra de Quilmes, all ranges within the swath profile (Fig. 1, 4) record protracted tectonic activity since the Pliocene (Strecker et al., 1989). Exhumation and uplift studies along the drier western flanks of Sierra Aconquija, for example, reveal that surface-uplift rates were on the order of 0.2 mm/yr during the early uplift history in Mio-Pliocene time, but increased up to 2 mm/yr by approximately 2 Ma (Sobel and Strecker, 2003). In contrast, in the same time frame exhumation rates decreased from 1 mm/yr to 0.2–0.3 mm/yr (Sobel and Strecker, 2003), similar to the rates based on cosmogenic nuclides observed in our study. This discrepancy in the long-term erosion rates has been explained with the fast removal of Tertiary sedimentary rocks covering Proterozoic basement during the early stages of uplift, followed by exposure of the less erodible basement rocks after the complete removal of the sediments. The low exhumation rates along the western slopes of Sierra Aconquija are compatible with inferred very low erosion rates of basement rocks in the adjacent Sierra de Quilmes (Fig. 1) immediately to the west. This range, which was uplifted after 6 Ma (Mortimer et al., 2007), exposes a well-preserved polycyclic, low-relief basement-erosion surface, which is locally covered by a 10.7-m.y.-old volcanic ash intercalated with sandstones (Strecker et al., 1989). The basement surface dips westward underneath Cenozoic basin sediments and causes a sharp contrast between the basement and the sedimentary rocks in the basin between this range and the ranges to the west that comprise the eastern border of the Altiplano-Puna Plateau. The basement surface is a hallmark of the morpho-tectonic characteristics of the Sierras Pampeanas basement-uplift province and has been preserved due to the aridity of this region.

Our analysis indicates that the concept of discharge-weighted specific stream power (or normalized steepness indices) is adequate to explain fluvial erosion rates measured on time scales represented by cosmogenic nuclides. Higher erosion rates may be affected by other erosion and transport processes (e.g., transient sediment storage, landsliding). We emphasize that drainage-area weighted specific stream power results in a weaker relationship ($r^2 = 0.4$), because of the steep climatic gradient in this region (Fig. 9).

5.3. Paleoclimatic impact

The comparison between erosion rates from different climatic zones of the orogen and the increase of basin-wide paleo-erosion rates in the semi-arid intermontane Calchaquí basin suggest that the steeper channel slopes in the dry areas of the southern Central Andes caused an amplified erosional signal during wetter periods in the past. This hypothesis is confirmed by re-evaluating the volume and chronology of the landslide-dam related sedimentary deposits at the outlet of the Calchaquíes basin. Based on the distribution and geometry of the lacustrine deposits paleo-erosion rates during the wet Minchin Phase were 10-fold higher than present-day cosmogenic-nuclide derived erosion rates. We interpret this signal to reflect higher transport and erosion rates of the steeper channels in the arid part of the orogen. Similar observations were reported from deposits associated with the early Holocene intensified monsoon phase in the western and central Himalaya (e.g., Bookhagen et al., 2005a; Pratt et al., 2002).

In addition, the disparity in the long-term erosional efficiency of surface processes on the wet versus dry sides of mountain ranges in the study region is well exemplified by the pronounced glacial morphology on the east-facing, humid slopes of Sierra Aconquija. These were subjected to a 1000-m depression of the Pleistocene snowline, reflected by extensive valley-glacier deposits and deeply carved valleys. In contrast, predominately cirque glaciations on the west-facing slopes were associated with a 400 m depression of the Pleistocene snowline of this range (Haselton et al., 2002). This asymmetry is also expressed in the evolution of drainage basins and the westward migration of the drainage divide in Sierra Aconquija (Bonnet, 2009).

6. Conclusions

The south Central Andes of northwestern Argentina are characterized by a steep climatic gradient that strongly influences erosion. Our analysis combines cosmogenic-nuclide erosion rates, field observations, topographic metrics, and satellite-data analysis to derive the following three key observations:

(1) Cosmogenic nuclide erosion rates exhibit a steep east-to-west gradient that largely mimics present-day mean annual rainfall across the Andes. Spatial variations of erosion can be best explained by a specific stream power approach that relies on discharge explicitly derived from calibrated, remotely sensed rainfall data. Discharge based on drainage area significantly overpredicts fluvial energy expenditure in the arid to semi-arid environments. Our data suggests that erosion rates of medium-sized drainage areas scale with specific stream power to the power of 1.4 up to erosion rates of 0.2 mm/yr, above which non-fluvial transport processes and transient sediment storage may become more dominant.

(2) Channel slopes in this threshold environment vary in concert with their climatic conditions. Compared to humid areas, arid areas require higher channel slopes to maintain equilibrium transport capacity. Only when investigating the discharge vs. channel slope relation the discrepancy disappears, suggesting that climate is an important landscape-controlling factor in this tectonically active region where exhumation rates are thought to be constant.

(3) Paleo-erosion rates in the areas that are dry today vary by one order of magnitude between the present-day and past episodes of greater moisture availability. Although the amount of our data is still limited, we show that during a wet phase corresponding to the Minchin lake highstand in the Bolivian Altiplano, erosion rates increased by a factor of 10 compared to catchment-mean erosion rates derived from cosmogenic nuclides. We explain this increase with the steeper channel slopes in the presently arid areas that amplify sediment transport when receiving enhanced moisture during periods with higher precipitation.

Acknowledgments

This research was partly financed by the DFG Leibniz Center for Earth Surface Process and Climate Studies (DFG grant STR373/19-19) at Potsdam University. The rainfall data were acquired as part of the Tropical Rainfall Measuring Mission (TRMM) sponsored by the Japan National Space Development Agency (NASDA) and the NASA. BB was supported with grants from NASA (NNX08AG05G) and NSF (EAR 0819874). We thank R. Alonso, T. Schildgen, B. Fisher, and D. Scherler for insightful discussions and suggestions. Furthermore, we thank N. Gasparini and an anonymous reviewer for insightful comments.

Appendix A. Supplementary data

Supplementary data to this article can be found online at doi:10.1016/j.epsl.2012.02.005.

References

Abbott, M.B., et al., 2003. Holocene paleohydrology and glacial history of the central Andes using multiproxy lake sediment studies. Palaeogeogr. Palaeoclimatol. Palaeoecol. 194 (1–3), 123–138.

Ahnert, F., 1970. Functional relationships between denudation, relief and uplift in large mid-latitude drainage basins. Am. J. Sci. 268, 243–263.

Anderson, R.S., 1994. Evolution of the Santa-Cruz Mountains, California, through tectonic growth and geomorphic decay. J. Geophys. Res.-Solid Earth 99 (B10), 20161–20179.
Bagnold, R.A., 1960. Sediment discharge and stream power, a preliminary announcement. U.S. Geol. Surv. Circ. U.S.G.S, p. 23.
Bagnold, R.A., 1977. Bed load transport by natural rivers. Water Resour. Res. 13 (2), 303–312.
Baker, P.A., et al., 2001. The history of South American tropical precipitation for the past 25,000 years. Science 291 (5504), 640–643.
Balco, G., et al., 2009. Regional beryllium-10 production rate calibration for late-glacial northeastern North America. Quatern. Geochronol. 4 (2), 93–107.
Beaumont, C., et al., 2001. Himalayan tectonics explained by extrusion of a low-viscosity crustal channel coupled to focused surface denudation. Nature 414 (6865), 738–742.
Bierman, P., Steig, E.J., 1996. Estimating rates of denudation using cosmogenic isotope abundances in sediment. Earth Surf. Process. Land. 21 (2), 125–139.
Binnie, S.A., et al., 2007. Tectonic uplift, threshold hillslopes, and denudation rates in a developing mountain range. Geology 35 (8), 743–746.
Bonnet, S., 2009. Shrinking and splitting of drainage basins in orogenic landscapes from the migration of the main drainage divide. Nat. Geosci. 2 (11), 766–771.
Bookhagen, B., Burbank, D.W., 2010. Toward a complete Himalayan hydrological budget: spatiotemporal distribution of snowmelt and rainfall and their impact on river discharge. J. Geophys. Res.-Earth Surf. 115.
Bookhagen, B., Strecker, M.R., 2008. Orographic barriers, high-resolution TRMM rainfall, and relief variations along the eastern Andes. Geophys. Res. Lett. 35 (6).
Bookhagen, B., et al., 2001. Hydrological modelling of a Pleistocene landslide-dammed lake in the Santa Maria basin, NW Argentina. Palaeogeogr. Palaeoclimatol. Palaeoecol. 169 (1–2), 113–127.
Bookhagen, B., et al., 2005a. Abnormal monsoon years and their control on erosion and sediment flux in the high, and northwest Himalaya. Earth Planet. Sci. Lett. 231 (1–2), 131–146.
Bookhagen, B., et al., 2005b. Late quaternary intensified monsoon phases control landscape evolution in the northwest Himalaya. Geology 33 (2), 149–152.
Bossi, G.E., et al., 2001. Cenozoic evolution of the intramontane Santa Maria basin, Pampean Ranges, northwestern Argentina. J. S. Am. Earth Sci. 14 (7), 725–734.
Burbank, D.W., et al., 1996. Bedrock incision, rock uplift and threshold hillslopes in the northwestern Himalayas. Nature 379 (6565), 505–510.
Burbank, D.W., et al., 2003. Decoupling of erosion and precipitation in the Himalayas. Nature 426 (6967), 652–655.
Carrapa, B., et al., 2008. Dynamics of deformation and sedimentation in the northern Sierras Pampeanas: an integrated study of the Neogene Fiambala basin, NW Argentina. Geol. Soc. Am. Bull. 120 (11–12), 1518–1543.
Clift, P.D., et al., 2008. Correlation of Himalayan exhumation rates and Asian monsoon intensity. Nat. Geosci. 1 (12), 875–880.
Cook, K.H., Vizy, E.K., 2006. South american climate during the last glacial maximum: delayed onset of the South American monsoon. J. Geophys. Res.-Atmospheres 111 (D2). doi:10.1029/2005JD005980.
Craddock, W.H., et al., 2007. Bedrock channel geometry along an orographic rainfall gradient in the upper Marsyandi River valley in central Nepal. J. Geophys. Res.-Earth Surf. 112 (F03007). doi:10.1029/2006JF000589.
Culling, W.E.H., 1960. Analytical theory of erosion. J. Geol. 68 (3), 336–344.
Cyr, A.J., et al., 2010. Quantifying rock uplift rates using channel steepness and cosmogenic nuclide-determined erosion rates: examples from northern and southern Italy. Lithosphere 2 (3), 188–198.
Dahlen, F.A., 1984. Noncohesive critical coulomb wedges — an exact solution. J. Geophys. Res. 89 (NB12), 125–133.
Davis, D., et al., 1983. Mechanics of fold-and-thrust belts and accretionary wedges. J. Geophys. Res. 88 (NB2), 1153–1172.
DiBiase, R.A., et al., 2010. Landscape form and millennial erosion rates in the San Gabriel Mountains, CA. Earth Planet. Sci. Lett. 289 (1–2), 134–144.
Eltahir, E.A.B., Bras, R.L., 1994. Precipitation recycling in the Amazon basin. Q. J. R. Meteorol. Soc. 120, 861–880.
Farr, T.G., et al., 2007. The shuttle radar topography mission. Rev. Geophys. 45 (RG2004). doi:10.1029/2005RG000183.
Finnegan, N.J., et al., 2005. Controls on the channel width of rivers: implications for modeling fluvial incision of bedrock. Geology 33 (3), 229–232.
Gilbert, G.K., 1877. Report on the Geology of the Henry Mountains. Government Printing Office, Washington, D.C.. 170 pp.
Granger, D.E., Muzikar, P.F., 2001. Dating sediment burial with in situ-produced cosmogenic nuclides: theory, techniques, and limitations. Earth Planet. Sci. Lett. 188 (1–2), 269–281.
Granger, D.E., et al., 1996. Spatially averaged long-term erosion rates measured from in situ-produced cosmogenic nuclides in alluvial sediment. J. Geol. 104 (3), 249–257.
Grier, M.E., et al., 1991. Andean reactivation of the Cretaceous Salta rift, northwestern Argentina. J. S. Am. Earth Sci. 4 (4), 351–372.
Grimm, A.M., et al., 2005. The South American monsoon system. In: Chang, C.P. (Ed.), The Global Monsoon System: Research and Forecast, pp. 219–238. WMO/TD No. 1266.
Hain, M.P., et al., 2011. Neogene to Quaternary broken-foreland formation and sedimentation dynamics in the Andes of NW Argentina (25°S). Tectonics 30.
Haselton, K., et al., 2002. Average Pleistocene climatic patterns in the Southern Central Andes: controls on mountain glaciation and paleoclimate implications. J. Geol. 110 (2), 211–226.
Heimsath, A.M., et al., 1997. The soil production function and landscape equilibrium. Nature 388, 358–361.
Hermanns, R.L., Schellenberger, A., 2008. Quaternary tephrochronology helps define conditioning factors and triggering mechanisms of rock avalanches in NW Argentina. Quatern. Int. 178, 261–275.
Hermanns, R.L., et al., 2000. Tephrochronologic constraints on temporal distribution of large landslides in northwest Argentina. J. Geol. 108 (1), 35–52.
Hilley, G.E., Coutand, I., 2010. Links between topography, erosion, rheological heterogeneity, and deformation in the contractional settings: insights from the central Andes. Tectonophysics 495, 78–92.
Hilley, G.E., Strecker, M.R., 2005. Processes of oscillatory basin filling and excavation in a tectonically active orogen: Quebrada del Toro Basin, NW Argentina. Geol. Soc. Am. Bull. 117 (7–8), 887–901.
Hodges, K.V., et al., 2004. Quaternary deformation, river steepening, and heavy precipitation at the front of the higher Himalayan ranges. Earth Planet. Sci. Lett. 220 (3–4), 379–389.
Hongn, F.D., Hippertt, J.F., 2001. Quartz crystallographic and morphologic fabrics during folding/transposition in mylonites. J. Struct. Geol. 23 (1), 81–92.
Hovius, N., et al., 1997. Sediment flux from a mountain belt derived by landslide mapping. Geology 25 (3), 231–234.
Howard, A.D., 1994. A detachment-limited model of drainage-basin evolution. Water Resour. Res. 30 (7), 2261–2285.
Howard, A.D., et al., 1994. Modeling fluvial erosion on regional to continental scales. J. Geophys. Res.-Solid Earth 99 (B7), 13971–13986.
Huffman, G.J., et al., 2007. The TRMM multisatellite precipitation analysis (TMPA): quasi-global, multiyear, combined-sensor precipitation estimates at fine scales. J. Hydrometeorology 8 (1), 38–55.
Insel, N., et al., 2010. Spatial and temporal variability in denudation across the Bolivian Andes from multiple geochronometers. Geomorphology 122 (1–2), 65–77.
Kirby, E., et al., 2003. Distribution of active rock uplift along the eastern margin of the Tibetan Plateau: inferences from bedrock channel longitudinal profiles. J. Geophys. Res.-Solid Earth 108 (B4).
Kirby, E., Whipple, K., 2001. Quantifying differential rock-uplift rates via stream profile analysis. Geology 29 (5), 415–418.
Kirchner, J.W., et al., 2001. Mountain erosion over 10 yr, 10 k.Y., and 10 m.Y. Time scales. Geology 29 (7), 591–594.
Knighton, A.D., 1999. Downstream variation in stream power. Geomorphology 29 (3–4), 293–306.
Kohl, C.P., Nishiizumi, K., 1992. Chemical isolation of quartz for measurement of insitu-produced cosmogenic nuclides. Geochim. Cosmochim. Acta 56 (9), 3583–3587.
Koons, P.O., 1989. The topographic evolution of collisional mountain belts — a numerical look at the Southern Alps, New-Zealand. Am. J. Sci. 289 (9), 1041–1069.
Koons, P.O., 1990. 2-sided orogen — collision and erosion from the sandbox to the Southern Alps, New-Zealand. Geology 18 (8), 679–682.
Lague, D., et al., 2005. Discharge, discharge variability, and the bedrock channel profile. J. Geophys. Res.-Earth Surf. 110 (F4).
Lague, D., Davy, P., 2003. Constraints on the long-term colluvial erosion law by analyzing slope-area relationships at various tectonic uplift rates in the Siwaliks Hills (Nepal). J. Geophys. Res.-Solid Earth 108 (B2).
Lal, D., 1991. Cosmic ray labeling of erosion surfaces: in situ nuclide production rates and erosion models. Earth and Planetary Science Letters 104, 424–439.
Marengo, J.A., et al., 2004. Climatology of the low-level jet east of the andes as derived from the NCEP–NCAR reanalyses: characteristics and temporal variability. J. Climate 17 (12), 2261–2280.
Markgraf, V., Seltzer, G.O., 2001. Pole-equator-pole Paleoclimates of the Americas Integration: Toward the Big Picture, in Interhemispheric Climate Linkages. In: Markgraf, V. (Ed.), Academic, San Diego, pp. 433–442.
Masek, J.G., et al., 1994. Erosion and tectonics at the margins of continental plateaus. J. Geophys. Res.-Solid Earth 99 (B7), 13941–13956.
Molnar, P., et al., 2007. Tectonics, fracturing of rock, and erosion. J. Geophys. Res.-Earth Surf. 112 (F3).
Molnar, P., England, P., 1990. Late cenozoic uplift of mountain-ranges and global climate change — chicken or egg? Nature 346 (6279), 29–34.
Mon, R., Hongn, F., 1991. The structure of the Precambrian and lower Paleozoic basement of the Central Andes between 22-degrees and 32-degrees S-lat. Geol. Rundsch. 80 (3), 745–758.
Mon, R., Salfity, J.A., 1995. Tectonic evolution of the Andes of northern Argentina. In: Tankard, A.J. (Ed.), Petroleum Basins of South America, Memoir. American Association of Petroleum Geologists.
Montgomery, D.R., Brandon, M.T., 2002. Topographic controls on erosion rates in tectonically active mountain ranges. Earth Planet. Sci. Lett. 201 (3–4), 481–489.
Mortimer, E., et al., 2007. Fragmentation of a foreland basin in response to out-of-sequence basement uplifts and structural reactivation: El Cajon-Campo del Arenal basin, NW Argentina. Geol. Soc. Am. Bull. 119 (5–6), 637–653.
Mu, Q., et al., 2007. Development of a global evapotranspiration algorithm based on modis and global meteorology data. Remote Sens. Environ. 111 (4), 519–536.
Niemi, N.A., et al., 2005. Effects of bedrock landslides on cosmogenically determined erosion rates. Earth Planet. Sci. Lett. 237 (3–4), 480–498.
Nishiizumi, K., et al., 2007. Absolute calibration of be-10 ams standards. Nucl. Instrum. Methods Phys. Res., Sect. B 258 (2), 403–413.
Ouimet, W.B., et al., 2009. Beyond threshold hillslopes: channel adjustment to base-level fall in tectonically active mountain ranges. Geology 37 (7), 579–582.
Placzek, C., et al., 2006. Geochronology and stratigraphy of Late Pleistocene lake cycles on the Southern Bolivian Altiplano: implications for causes of tropical climate change. Geol. Soc. Am. Bull. 118 (5–6), 515–532.
Pratt, B., et al., 2002. Impulsive alluviation during early Holocene strengthened monsoons, central Nepal Himalaya. Geology 30 (10), 911–914.
Ramos, V.A., 2008. The basement of the Central Andes: the Arequipa and related terranes. Annu. Rev. Earth Planet. Sci. 36, 289–324.
Rao, V.B., et al., 1996. Annual variation of rainfall over Brazil and water vapor characteristics over South America. J. Geophys. Res.-Atmospheres 101 (D21), 26539–26551.

Reiners, P.W., et al., 2003. Coupled spatial variations in precipitation and long-term erosion rates across the Washington Cascades. Nature 426 (6967), 645–647.
Schaller, M., Ehlers, T.A., 2006. Limits to quantifying climate driven changes in denudation rates with cosmogenuc radionuclides. Earth Planet. Sci. Lett. 248, 138–152.
Schaller, M., et al., 2001. Large-scale erosion rates from in situ-produced cosmogenic nuclides in European river sediments. Earth Planet. Sci. Lett. 188 (3–4), 441–458.
Schwerdtfeger, W., 1976. Climates of Central and South America. Elsevier Scientific Publishing, Amsterdam, The Netherlands. 532 pp.
Seltzer, G.O., et al., 2003. Late-quaternary paleoclimates of the southern tropical Andes and adjacent regions. Palaeogeogr. Palaeoclimatol. Palaeoecol. 194, 1–3.
Seluchi, M.E., et al., 2003. The Northwestern Argentinean low: a study of two typical events. Mon. Weather Rev. 131 (10), 2361–2378.
Sklar, L.S., Dietrich, W.E., 2004. A mechanistic model for river incision into bedrock by saltating bed load. Water Resour. Res. 40 (6).
Snyder, N.P., et al., 2003. Importance of a stochastic distribution of floods and erosion thresholds in the bedrock river incision problem. J. Geophys. Res.-Solid Earth 108 (B2).
Sobel, E.R., Strecker, M.R., 2003. Uplift, exhumation and precipitation: tectonic and climatic control of Late Cenozoic landscape evolution in the northern Sierras Pampeanas, Argentina. Basin Res. 15 (4), 431–451.
Strecker, M.R., et al., 1989. Late cenozoic tectonism and landscape development in the foreland of the andes — northern Sierras Pampeanas (26–28 degrees S), Argentina. Tectonics 8 (3), 517–534.
Strecker, M.R., et al., 2007. Tectonics and climate of the Southern Central Andes. Annu. Rev. Earth Planet. Sci. 35, 747–787.
Thiede, R.C., et al., 2009. Erosional variability along the northwest Himalaya. J. Geophys. Res.-Earth Surf. 114.
Thiede, R.C., et al., 2004. Climatic control on rapid exhumation along the Southern Himalayan Front. Earth Planet. Sci. Lett. 222 (3–4), 791–806.
Trauth, M.H., Strecker, M.R., 1999. Formation of landslide-dammed lakes during a wet period between 40,000 and 25,000 yr bp in northwestern Argentina. Palaeogeogr. Palaeoclimatol. Palaeoecol. 153 (1–4), 277–287.
Trauth, M.H., et al., 2000. Climate change and mass movements in the NW Argentine Andes. Earth Planet. Sci. Lett. 179 (2), 243–256.
Trauth, M.H., et al., 2003. Late pleistocene climate change and erosion in the Santa Maria basin, NW Argentina. J. Sed. Res. 73 (1), 82–90.
Tucker, G.E., Bras, R.L., 1998. Hillslope processes, drainage density, and landscape morphology. Water Resour. Res. 34 (10), 2751–2764.
Tucker, G.E., Slingerland, R., 1997. Drainage basin responses to climate change. Water Resour. Res. 33 (8), 2031–2047.
Vera, C., et al., 2006. Toward a unified view of the American monsoon systems. J. Climate 19 (20), 4977–5000.
Viramonte, J.G., et al., 1999. Cretaceous rift related magmatism in central-western South America. J. S. Am. Earth Sci. 12 (2), 109–121.
Vizy, E.K., Cook, K.H., 2007. Relationship between Amazon and high Andes rainfall. J. Geophys. Res.-Atmospheres 112 (D7).
von Blanckenburg, F., et al., 2004. Cosmogenic nuclide evidence for low weathering and denudation in the wet, tropical highlands of Sri Lanka. J. Geophys. Res.-Earth Surf. 109 (F3).
von Blanckenburg, F., 2005. The control mechanisms of erosion and weathering at basin scale from cosmogenic nuclides in river sediment. Earth Planet. Sci. Lett. 237 (3–4), 462–479.
Whipple, K.X., 2004. Bedrock rivers and the geomorphology of active orogens. Annu. Rev. Earth Planet. Sci. 32, 151–185.
Whipple, K.X., 2009. The influence of climate on the tectonic evolution of mountain belts. Nat. Geosci. 2 (2), 97–104.
Whipple, K.X., Meade, B.J., 2006. Orogen response to changes in climatic and tectonic forcing. Earth Planet. Sci. Lett. 243 (1–2), 218–228.
Whipple, K.X., et al., 1999. Geomorphic limits to climate-induced increases in topographic relief. Nature 401 (6748), 39–43.
Whittaker, A.C., et al., 2007. Bedrock channel adjustment to tectonic forcing: implications for predicting river incision rates. Geology 35 (2), 103–106.
Willett, S.D., 1999. Orogeny and orography: the effects of erosion on the structure of mountain belts. J. Geophys. Res.-Solid Earth 104 (B12), 28957–28981.
Willett, S.D., Brandon, M.T., 2002. On steady states in mountain belts. Geology 30 (2), 175–178.
Wobus, C., et al., 2006. Tectonics from topography: procedures, promise, and pitfalls. In: Willett, S.D. (Ed.), Tectonics, Climate, and Landscape Evolution: Geological Society of America Special Paper, 398, pp. 55–74.
Yanites, B.J., Tucker, G.E., 2010. Controls and limits on bedrock channel geometry. J. Geophys. Res.-Earth Surf. 115.
Zhou, J.Y., Lau, K.M., 1998. Does a monsoon climate exist over South America? J. Climate 11 (5), 1020–1040.